Wind Energy

WIND ENERGY
Wind Energ. (2017)
Published online in Wiley Online Library (wileyonlinelibrary.com). DOI: 10.1002/we.2101

RESEARCH ARTICLE

BeamDyn: a high-fidelity wind turbine blade solver in the FAST modular framework

Qi Wang[1], Michael A. Sprague[1], Jason Jonkman[1], Nick Johnson[2] and Bonnie Jonkman[1]

[1] National Renewable Energy Laboratory, 15013 Denver West Parkway, Golden, CO 80401, USA
[2] Department of Mechanical Engineering, Colorado School of Mines, Golden, CO 80401, USA

ABSTRACT

This paper presents a numerical implementation of the geometrically exact beam theory based on the Legendre-spectral-finite-element (LSFE) method. The displacement-based geometrically exact beam theory is presented, and the special treatment of three-dimensional rotation parameters is reviewed. An LSFE is a high-order finite element with nodes located at the Gauss–Legendre–Lobatto points. These elements can be an order of magnitude more computationally efficient than low-order finite elements for a given accuracy level. The new module, BeamDyn, is implemented in the FAST modularization framework for dynamic simulation of highly flexible composite-material wind turbine blades within the FAST aeroelastic engineering model. The framework allows for fully interactive simulations of turbine blades in operating conditions. Numerical examples are provided to validate BeamDyn and examine the LSFE performance as well as the coupling algorithm in the FAST modularization framework. BeamDyn can also be used as a stand-alone high-fidelity beam tool. Copyright © 2017 John Wiley & Sons, Ltd.

KEYWORDS
geometrically exact beam theory; Legendre spectral finite element; wind turbine analysis; structural dynamics; FAST

Correspondence
Q. Wang, 1050 Walnut Street, Boulder, CO 80302-5142, USA and Michael A. Sprague, National Renewable Energy Laboratory, 15013 Denver West Parkway, Golden, CO 80401, USA.
E-mail: wangqi315@hotmail.com; michael.a.sprague@nrel.gov

Received 14 June 2016; Revised 19 November 2016; Accepted 11 February 2017

Wind power is becoming one of the most important renewable energy sources in the USA. In recent years, the size of wind turbines has been increasing immensely to lower the cost of energy, which, because of weight restrictions, requires highly flexible turbine blades. This huge electromechanical system poses a significant challenge for engineering design and analysis. Although possible with modern super computers, direct three-dimensional (3-D) structural analysis is so computationally expensive that engineers are always seeking for more efficient, highly accurate models, especially in the context of coupled aeroelastics.

Beam models are widely used to represent and analyse engineering structures that have one dimension that is much larger than the other two. Many engineering components can be idealized as beams: structural members of buildings and bridges in civil engineering, joists and lever arms in heavy-machine industries and helicopter rotor blades. The blades, tower and shaft in a wind turbine system can be analysed as beams. In the weight-critical applications of beam structures, like high-aspect-ratio wings in aerospace and wind energy applications, composite materials are attractive because of their superior strength-to-weight and stiffness-to-weight ratios. However, analysis of composite-material structures is more difficult than their isotropic counterparts due to elastic-coupling effects. Furthermore, wind turbine blades are further complicated by their high flexibility and initial twist/curvatures, which must be treated in the underlying analysis. The geometrically exact beam theory (GEBT), first proposed by Reissner,[1] is a method that has proven powerful for analysis of highly flexible composite beams in the helicopter engineering community. During the past several decades, much effort has been invested in GEBT. Simo[2] and Simo and Vu-Quoc[3] extended Reissner's work to deal with 3-D dynamic problems. Jelenić and Crisfield[4] implemented GEBT using the finite-element method in which a new approach for interpolating the rotation field was proposed that preserves the geometric exactness. Betsch and Steinmann[5] circumvented the interpolation of rotation by introducing a re-parameterization of the weak form corresponding to the equations of motion of GEBT. Ibrahimbegović[6] implemented GEBT for static analysis, and Ibrahimbegović and Mikdad[7] implemented GEBT for

Copyright © 2017 John Wiley & Sons, Ltd.

Pursuant to the DOE Public Access Plan, this document represents the authors' peer-reviewed, accepted manuscript.
The published version of the article is available from the relevant publisher.

dynamic analysis. In contrast to the displacement-based implementations, Hodges[8] proposed a discretization of the GEBT model with mixed finite elements in which both the primary and dual fields are independently interpolated.[9] In the mixed formulation, all of the necessary ingredients, including Hamilton's principle and kinematic equations, are combined in a single variational formulation statement. Lagrange multipliers, motion variables, generalized strains, forces and moments, linear and angular momenta, and displacement and rotation variables are considered as independent quantities. Yu and Blair[10] and Wang *et al.*[11] recently presented the implementation of GEBT in a mixed formulation in which various rotation parameters were investigated and the authors' codes were validated against analytical and numerical solutions.

For complex beam structures, e.g., those with complicated composite lay-ups or cross-section geometry, a proper preprocessor is needed for beam solvers to provide the cross-sectional properties at different stations along a beam's span. The accuracy of the global beam analysis is heavily dependent on these properties, especially for composite-material beams. There are several popular cross-sectional preprocessors, including PreComp,[12] VABS,[13] BECAS[14] and NuMAD.[15] PreComp, which is based on a thin-walled classical laminate theory, was developed for early state design with relatively low accuracy. VABS and BECAS are high-fidelity modeling tools that are appropriate for turbine blade design and analysis. Introduction and review of the cross-section analysis tools for wind energy applications can be found in Hodges and Yu[16] and Chen *et al.*[17] For comprehensive derivations and discussions on nonlinear composite-beam theories, see Hodges.[18]

Legendre spectral finite elements[19,20] (LSFEs) are *p*-type finite elements whose shape functions are Lagrangian interpolants with node locations at the Gauss–Lobatto–Legendre points. LSFEs combine the accuracy of global spectral methods with geometric flexibility of *h*-type finite elements. The spectral finite elements have been successfully used in the simulation of fluid dynamics,[19–21] two-dimensional elastic wave propagation in solid media in geophysics,[22] elastodynamics[23] and acoustic wave propagation.[24] However, there has been limited application of these elements to dynamic analysis of beam[25,26] and plate elements.[27–29] Sprague and Purkayastha[29] showed that, for static and dynamic analyses of composite-material plates, LSFEs can provide orders of magnitude of greater accuracy, for either a given model size or computation time, when compared with common low-order elements.

FAST is an open-source computer-aided engineering and analysis tool developed by the National Renewable Energy Laboratory (NREL) for analysing both land-based and offshore wind turbines under realistic operating conditions. The beam model provided in the ElastoDyn FAST module is not capable of predictive analysis of highly flexible, composite wind turbine blades. Recently, FAST has been reformulated under a new modularized framework that provides a rigorous means by which various mathematical systems are implemented in distinct modules. These modules are interconnected to solve for the globally coupled dynamic responses of wind turbines[30,31] and wind plants.[32] In addition to FAST, there are several other aero-structural analysis tools currently used in the wind energy research community and industry.

The blade models in FLEX,[33] Bladed[34] and the FAST ElastoDyn module are based on an assumed-mode method for straight Euler–Bernoulli beams with bending only. While some geometric nonlinearities are included, their solutions are limited to moderate deflections. The blade models of HAWC2[35] and multibody Bladed are based on a combined multibody and linear generalized Timoshenko finite-element representation, allowing for geometric nonlinearities through a series of multiple bodies (via geometric constraints), each composed of linear finite elements. In contrast, the BeamDyn model enables the solution of the generalized Timoshenko beam and full geometric nonlinearity with a single finite element without the need to solve separate constraint equations. A strain-based implementation of GEBT by Su and Cesnik[36] was also applied to wind turbine analysis.[37]

The rest of this paper is organized as follows. Section 1 reviews the GEBT and linearization of the governing equations. Section 2 describes the LSFE and other numerical tools adopted in the implementation of BeamDyn, including Wiener–Milenković rotation parameters, numerical integration and the module coupling algorithm. Validation examples are presented in Section 3, and concluding remarks are given in Section 4.

1. GEOMETRICALLY EXACT BEAM THEORY

For completeness, this section reviews the GEBT and linearization process of the governing equations. The content of this section can be found in many other places (e.g., Bauchau[38]). Figure 1[8,18] shows a beam in its undeformed and deformed states. A reference frame $\mathbf{b}_i$ is introduced along the beam axis for the undeformed state; a frame $\mathbf{B}_i$ is introduced along each point of the deformed beam axis. Curvilinear coordinate x_1 defines the intrinsic parameterization of the reference line. In this paper, we use matrix notation to denote vectorial or vectorial-like quantities. For example, we use an underline to denote a vector, e.g., $\underline{u}$, a bar to denote unit vector, e.g., $\bar{n}$, and double underline to denote a tensor, e.g., $\underline{\underline{\Delta}}$. Note that sometimes the underlines only denote the dimension of the corresponding matrix. The governing equations of motion for geometric exact beam theory can be written as[38]

$$\dot{\underline{h}} - \underline{F}' = \underline{f} \tag{1}$$

$$\dot{\underline{g}} + \dot{\tilde{u}}\underline{h} - \underline{M}' - (\tilde{x}_0' + \tilde{u}')\underline{F} = \underline{m} \tag{2}$$

Pursuant to the DOE Public Access Plan, this document represents the authors' peer-reviewed, accepted manuscript.
The published version of the article is available from the relevant publisher.

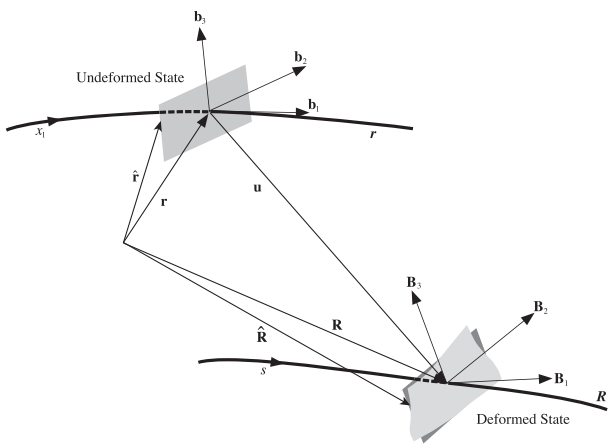

Figure 1. Schematic of the beam in undeformed and deformed states with associated variables.

where $\underline{h}$ and $\underline{g}$ are the linear and angular momenta resolved in the inertial coordinate system, respectively, $\underline{F}$ and $\underline{M}$ are the beam's sectional forces and moments, respectively, $\underline{u}$ is the one-dimensional displacement of the reference line, $\underline{x}_0$ is the initial position vector of a point along the beam's reference line, and $\underline{f}$ and $\underline{m}$ are the distributed force and moment applied to the beam structure, respectively. Notation $(\cdot)'$ indicates a derivative with respect to the beam axis x_1, and $(\dot{\cdot})$ indicates a derivative with respect to time. The tilde operator $\widetilde{(\cdot)}$ defines a second-order, skew-symmetric tensor corresponding to the given vector. In the literature, it is also termed as 'cross-product matrix'. For example,

$$\widetilde{n} = \begin{bmatrix} 0 & -n_3 & n_2 \\ n_3 & 0 & -n_1 \\ -n_2 & n_1 & 0 \end{bmatrix} \tag{3}$$

The constitutive equations relate the velocities to the momenta and the one-dimensional strain measures to the sectional resultants as

$$\begin{Bmatrix} \underline{h} \\ \underline{g} \end{Bmatrix} = \underline{\underline{\mathcal{M}}} \begin{Bmatrix} \dot{\underline{u}} \\ \underline{\omega} \end{Bmatrix} \tag{4}$$

$$\begin{Bmatrix} \underline{F} \\ \underline{M} \end{Bmatrix} = \underline{\underline{\mathcal{C}}} \begin{Bmatrix} \underline{\epsilon} \\ \underline{\kappa} \end{Bmatrix} \tag{5}$$

where $\underline{\underline{\mathcal{M}}}$ and $\underline{\underline{\mathcal{C}}}$ are the 6×6 sectional mass and stiffness matrices, respectively (note that they are not tensors), and $\underline{\epsilon}$ and $\underline{\kappa}$ are the one-dimensional strains and curvatures, respectively. $\underline{\omega}$ is the angular velocity vector that is defined by the rotation tensor $\underline{\underline{R}}$ as $\underline{\omega} = \text{axial}(\dot{\underline{\underline{R}}}\,\underline{\underline{R}})$.

For a displacement-based finite-element implementation, there are six degrees of freedom at each node: three displacement components and three rotation components. Here, we use $\underline{q}$ to denote the elemental displacement array as $\underline{q} = \left[\underline{u}^T \;\; \underline{p}^T\right]$, where $\underline{u}$ is the one-dimensional displacement and $\underline{p}$ is the rotation parameter vector. The acceleration array can thus be defined as $\underline{a} = \left[\ddot{\underline{u}}^T \;\; \dot{\underline{\omega}}^T\right]$. For nonlinear finite-element analysis, the discretized and incremental forms of displacement, velocity and acceleration are written as

$$\underline{q}(x_1) = \underline{\underline{N}}\,\hat{\underline{q}} \quad \Delta\underline{q}^T = \left[\Delta\underline{u}^T \;\; \Delta\underline{p}^T\right] \tag{6}$$

$$\underline{v}(x_1) = \underline{\underline{N}}\,\hat{\underline{v}} \quad \Delta\underline{v}^T = \left[\Delta\dot{\underline{u}}^T \;\; \Delta\underline{\omega}^T\right] \tag{7}$$

$$\underline{a}(x_1) = \underline{\underline{N}}\,\hat{\underline{a}} \quad \Delta\underline{a}^T = \left[\Delta\ddot{\underline{u}}^T \;\; \Delta\dot{\underline{\omega}}^T\right] \tag{8}$$

where $\underline{\underline{N}}$ is the shape function matrix and $(\hat{\cdot})$ denotes a column matrix of nodal values. The governing equations for beams are highly nonlinear so that a linearization process is needed. According to Bauchau,[38] the linearized governing equations in equations (1) and (2) are in the form of

$$\underline{\underline{\hat{M}}}\Delta\hat{\underline{a}} + \underline{\underline{\hat{G}}}\Delta\hat{\underline{v}} + \underline{\underline{\hat{K}}}\Delta\hat{\underline{q}} = \hat{\underline{F}}^{ext} - \hat{\underline{F}} \tag{9}$$

Pursuant to the DOE Public Access Plan, this document represents the authors' peer-reviewed, accepted manuscript.
The published version of the article is available from the relevant publisher.

where $\underline{\underline{\hat{M}}}$, $\underline{\underline{\hat{G}}}$ and $\underline{\underline{\hat{K}}}$ are the elemental mass, gyroscopic and stiffness matrices, respectively, and $\underline{\hat{F}}$ and $\underline{\hat{F}}^{ext}$ are the elemental forces and externally applied loads, respectively. They are defined as follows:

$$\underline{\underline{\hat{M}}} = \int_0^l \underline{\underline{N}}^T \underline{\underline{\mathcal{M}}}\, \underline{\underline{N}} dx_1 \tag{10}$$

$$\underline{\underline{\hat{G}}} = \int_0^l \underline{\underline{N}}^T \underline{\underline{\mathcal{G}}}^I\, \underline{\underline{N}} dx_1 \tag{11}$$

$$\underline{\underline{\hat{K}}} = \int_0^l \left[\underline{\underline{N}}^T (\underline{\underline{\mathcal{K}}}^I + \underline{\underline{\mathcal{Q}}})\, \underline{\underline{N}} + \underline{\underline{N}}^T \underline{\underline{\mathcal{P}}}\, \underline{\underline{N}}' + \underline{\underline{N}}'^T \underline{\underline{\mathcal{C}}}\, \underline{\underline{N}}' + \underline{\underline{N}}'^T \underline{\underline{\mathcal{O}}}\, \underline{\underline{N}}\right] dx_1 \tag{12}$$

$$\underline{\hat{F}} = \int_0^l (\underline{\underline{N}}^T \underline{\mathcal{F}}^I + \underline{\underline{N}}^T \underline{\mathcal{F}}^D + \underline{\underline{N}}'^T \underline{\mathcal{F}}^C) dx_1 \tag{13}$$

$$\underline{\hat{F}}^{ext} = \int_0^l \underline{\underline{N}}^T \underline{\mathcal{F}}^{ext} dx_1 \tag{14}$$

The new matrix notations in equations (10) to (14) are briefly introduced here. $\underline{\underline{\mathcal{M}}}$ is the sectional mass matrix resolved in inertial system; $\underline{\mathcal{F}}^C$ and $\underline{\mathcal{F}}^D$ are elastic forces obtained from equations (1) and (2) as

$$\underline{\mathcal{F}}^C = \begin{Bmatrix} \underline{F} \\ \underline{M} \end{Bmatrix} = \underline{\underline{\mathcal{C}}} \begin{Bmatrix} \underline{\epsilon} \\ \underline{\kappa} \end{Bmatrix} \tag{15}$$

$$\underline{\mathcal{F}}^D = \begin{bmatrix} \underline{\underline{0}} & \underline{\underline{0}} \\ (\underline{x}_0' + \underline{u}')^T & \underline{\underline{0}} \end{bmatrix} \underline{\mathcal{F}}^C \equiv \underline{\underline{\Upsilon}}\, \underline{\mathcal{F}}^C \tag{16}$$

where $\underline{\underline{0}}$ denotes a 3×3 null matrix. $\underline{\underline{\mathcal{G}}}^I$, $\underline{\underline{\mathcal{K}}}^I$, $\underline{\underline{\mathcal{O}}}$, $\underline{\underline{\mathcal{P}}}$, $\underline{\underline{\mathcal{Q}}}$ and $\underline{\mathcal{F}}^I$ in equations (11)–(13) are defined as

$$\underline{\underline{\mathcal{G}}}^I = \begin{bmatrix} \underline{\underline{0}} & (\tilde{\omega} m \underline{\eta})^T + \tilde{\omega} m \tilde{\eta}^T \\ \underline{\underline{0}} & \tilde{\tilde{\omega}} \underline{\underline{\varrho}} - \widetilde{\underline{\underline{\varrho}}\,\underline{\omega}} \end{bmatrix} \tag{17}$$

$$\underline{\underline{\mathcal{K}}}^I = \begin{bmatrix} \underline{\underline{0}} & \dot{\tilde{\omega}} m \tilde{\eta}^T + \tilde{\omega}\tilde{\omega} m \tilde{\eta}^T \\ \underline{\underline{0}} & \ddot{\underline{u}} m \tilde{\eta} + \underline{\underline{\varrho}}\dot{\tilde{\omega}} - \widetilde{\underline{\underline{\varrho}}\,\dot{\underline{\omega}}} + \tilde{\omega}\underline{\underline{\varrho}}\tilde{\omega} - \tilde{\omega}\widetilde{\underline{\underline{\varrho}}\,\underline{\omega}} \end{bmatrix} \tag{18}$$

$$\underline{\underline{\mathcal{O}}} = \begin{bmatrix} \underline{\underline{0}} & \underline{\underline{C}}_{11}\tilde{E}_1 - \tilde{F} \\ \underline{\underline{0}} & \underline{\underline{C}}_{21}\tilde{E}_1 - \tilde{M} \end{bmatrix} \tag{19}$$

$$\underline{\underline{\mathcal{P}}} = \begin{bmatrix} \underline{\underline{0}} & \underline{\underline{0}} \\ \tilde{F} + (\underline{\underline{C}}_{11}\tilde{E}_1)^T & (\underline{\underline{C}}_{21}\tilde{E}_1)^T \end{bmatrix} \tag{20}$$

$$\underline{\underline{\mathcal{Q}}} = \underline{\underline{\Upsilon}}\, \underline{\underline{\mathcal{O}}} \tag{21}$$

$$\underline{\mathcal{F}}^I = \begin{Bmatrix} m\ddot{\underline{u}} + (\dot{\tilde{\omega}} + \tilde{\omega}\tilde{\omega}) m \underline{\eta} \\ m\tilde{\eta}\ddot{\underline{u}} + \underline{\underline{\varrho}}\dot{\underline{\omega}} + \tilde{\omega}\underline{\underline{\varrho}}\underline{\omega} \end{Bmatrix} \tag{22}$$

where m is the mass density per unit length, $\underline{\eta}$ is the location of the sectional center of mass, $\underline{\underline{\varrho}}$ is the moment of inertia tensor per unit length and the following notations were introduced to simplify the writing of the aforementioned expressions:

$$\underline{E}_1 = \underline{x}_0' + \underline{u}' \tag{23}$$

$$\underline{\underline{\mathcal{C}}} = \begin{bmatrix} \underline{\underline{C}}_{11} & \underline{\underline{C}}_{12} \\ \underline{\underline{C}}_{21} & \underline{\underline{C}}_{22} \end{bmatrix} \tag{24}$$

A viscous damping term is also implemented to account for the structural damping. The damping force is defined as

$$\underline{f}_d = \underline{\underline{\mu}}\, \underline{\underline{\mathcal{C}}} \begin{Bmatrix} \dot{\epsilon} \\ \dot{\kappa} \end{Bmatrix} \tag{25}$$

where $\underline{\underline{\mu}}$ is a user-provided damping-coefficient diagonal matrix. The damping force can be recast in two separate parts, like $\underline{\mathcal{F}}^{\overline{\overline{C}}}$ and $\underline{\mathcal{F}}^D$ in the elastic force, as

Pursuant to the DOE Public Access Plan, this document represents the authors' peer-reviewed, accepted manuscript.
The published version of the article is available from the relevant publisher.

$$\underline{\mathcal{F}}_d^C = \begin{Bmatrix} \underline{F}_d \\ \underline{M}_d \end{Bmatrix} \tag{26}$$

$$\underline{\mathcal{F}}_d^D = \begin{Bmatrix} \underline{0} \\ (\tilde{x}_0' + \tilde{u}')^T \underline{F}_d \end{Bmatrix} \tag{27}$$

More details on the derivation and linearization of governing equations of GEBT can be found in Bauchau.[38]

2. NUMERICAL IMPLEMENTATION

2.1. Wiener–Milenković rotation parameters

The 3-D rotations in BeamDyn are represented as Wiener–Milenković parameters,[11,39] which are defined as

$$\underline{p} = 4 \tan\left(\frac{\phi}{4}\right) \bar{n} \tag{28}$$

where ϕ is the rotation angle and $\bar{n}$ is the unit vector of the rotation axis. It can be observed that the valid range for this parameter is $|\phi| < 2\pi$. The singularities existing at integer multiples of $\pm 2\pi$ can be removed by a rescaling operation at π, as given in Bauchau *et al.*[39]

$$\underline{r} = \begin{cases} 4(q_0\underline{p} + p_0\underline{q} + \tilde{p}\underline{q})/(\Delta_1 + \Delta_2), & \text{if } \Delta_2 \geq 0 \\ -4(q_0\underline{p} + p_0\underline{q} + \tilde{p}\underline{q})/(\Delta_1 - \Delta_2), & \text{if } \Delta_2 < 0 \end{cases} \tag{29}$$

where $\underline{p}$, $\underline{q}$ and $\underline{r}$ are the vectorial parameterization of three finite rotations such that $\underline{\underline{R}}(\underline{r}) = \underline{\underline{R}}(\underline{p})\underline{\underline{R}}(\underline{q})$, $p_0 = 2 - \underline{p}^T\underline{p}/8$, $q_0 = 2 - \underline{q}^T\underline{q}/8$, $\Delta_1 = (4 - p_0)(4 - q_0)$ and $\Delta_2 = p_0 q_0 - \underline{p}^T\underline{q}$. It is noted that the rescaling operation could cause a discontinuity of the interpolated rotation field. Therefore, a more robust interpolation algorithm is introduced where the rescaling-independent relative-rotation field is interpolated.

The displacement fields in an element are approximated as

$$\underline{u}(\xi) = \sum_{k=1}^{p+1} h^k(\xi)\hat{\underline{u}}^k \tag{30}$$

$$\underline{u}'(\xi) = \sum_{k=1}^{p+1} h^{k\prime}(\xi)\hat{\underline{u}}^k \tag{31}$$

where $h^k(\xi)$, a component of shape-function matrix $\underline{\underline{N}}$, is the pth-order-polynomial Lagrangian-interpolant shape function of node k, $k = \{1, 2, \ldots, p+1\}$, $\hat{\underline{u}}^k$ is the kth nodal value and $\xi \in [-1, 1]$ is the element natural coordinate. However, as discussed in Bauchau *et al.*,[39] the 3-D rotation field cannot simply be interpolated as the displacement field in the form of

$$\underline{c}(\xi) = \sum_{k=1}^{p+1} h^k(\xi)\hat{\underline{c}}^k \tag{32}$$

$$\underline{c}'(\xi) = \sum_{k=1}^{p+1} h^{k\prime}(\xi)\hat{\underline{c}}^k \tag{33}$$

where $\underline{c}$ is the rotation field in an element and $\hat{\underline{c}}^k$ is the nodal value at the kth node, for three reasons: (i) rotations do not form a linear space so that they must be 'composed' rather than added, (ii) a rescaling operation is needed to eliminate the singularity existing in the vectorial rotation parameters and (iii) the rotation field lacks objectivity, which, as defined by Jelenić and Crisfield,[4] refers to the invariance of strain measures computed through interpolation to the addition of a rigid-body motion. Therefore, we adopt the more robust interpolation approach proposed by Jelenić and Crisfield[4] to deal with the finite rotations. Our approach is described as follows.

Step 1: Compute the nodal relative rotations, $\hat{\underline{r}}^k$, by removing the reference rotation, $\hat{\underline{c}}^1$, from the finite rotation at each node, $\hat{\underline{r}}^k = (\hat{\underline{c}}^{1-}) \oplus \hat{\underline{c}}^k$. Note that the minus sign on $\hat{\underline{c}}^1$ denotes that the relative rotation is calculated by removing the reference rotation from each node. The composition in that equation is an equivalent of $\underline{\underline{R}}(\hat{\underline{r}}^k) = \underline{\underline{R}}^T(\hat{\underline{c}}^1)\,\underline{\underline{R}}(\underline{c}^k)$.

Pursuant to the DOE Public Access Plan, this document represents the authors' peer-reviewed, accepted manuscript.
The published version of the article is available from the relevant publisher.

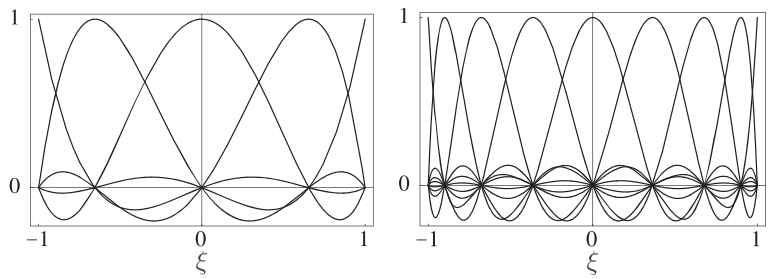

(a) $p = 4$ **(b)** $p = 8$

Figure 2. Representative $p + 1$ Lagrangian-interpolant shape functions in the element natural coordinates for (a) fourth-order and (b) eighth-order LSFEs, where nodes are located at the Gauss–Lobatto–Legendre points.

Step 2: Interpolate the relative-rotation field: $\underline{r}(\xi) = h^k(\xi)\hat{\underline{r}}^k$ and $\underline{r}'(\xi) = h^{k\prime}(\xi)\hat{\underline{r}}^k$. Find the curvature field $\underline{\kappa}(\xi) = \underline{\underline{R}}(\hat{\underline{c}}^1)\underline{\underline{H}}(\underline{r})\underline{r}'$, where $\underline{\underline{H}}$ is the tangent tensor that relates the curvature vector $\underline{k}$ and rotation vector $\underline{p}$ as

$$\underline{k} = \underline{\underline{H}}\,\underline{p}' \tag{34}$$

Step 3: Restore the rigid-body rotation removed in Step 1: $\underline{c}(\xi) = \hat{\underline{c}}^1 \oplus \underline{r}(\xi)$.

Note that the relative-rotation field can be computed with respect to any of the nodes of the element; we choose node 1 as the reference node for convenience. For the Wiener–Milenković rotation parameter, the tangent vector $\underline{\underline{H}}$ is defined as follows:

$$\underline{\underline{H}}(\underline{c}) = \frac{2}{(4 - c_0)^2}\left[c_0 + \tilde{c} + \frac{1}{4}\underline{c}\underline{c}^T\right] \tag{35}$$

where

$$c_0 = 2 - \frac{1}{8}\underline{c}^T\underline{c} \tag{36}$$

2.2. Legendre spectral finite elements

In the LSFE approach, shape functions (i.e., those composing $\underline{\underline{N}}$) are pth-order Lagrangian interpolants, where nodes are located at the $p + 1$ Gauss–Lobatto–Legendre points in the $[-1, 1]$ element natural-coordinate domain. Figure 2 shows representative LSFE basis functions for fourth-order and eighth-order elements. Note that nodes are clustered near element end points.

2.3. Numerical integration

Numerical integration (quadrature) of the finite-element inner products over an element domain is required in the finite-element formulation. Typically, the quadrature rule employed in a finite-element implementation is Gauss–Legendre, for which the number of quadrature points is chosen based on the polynomial order of the underlying finite-element basis functions. In the case in which material properties or applied loads vary significantly over an element domain, the accuracy of the quadrature is degraded, which can affect the overall accuracy of the solution. If the number of quadrature points is fixed to the finite-element basis-function order, accuracy is increased by either increasing the number of elements (h-refinement) or the order of the elements (p-refinement). However, if the quadrature order is chosen for accurate evaluation of finite-element inner products, then the choice in finite-element resolution can be based on overall solution accuracy.

For wind turbine blade analysis, material sectional properties are defined discretely at n_s stations along the beam axis. BeamDyn is equipped with two quadrature options: Gauss–Legendre quadrature and trapezoidal-rule quadrature, where the latter is only enabled when the blade is represented as a *single* element. For Gauss–Legendre quadrature, BeamDyn requires that $n_q = p+1$, where n_q is the number of quadrature points and p is the order of the LSFE. Material properties are linearly interpolated to quadrature-point locations from the nearest stations. For a modern wind turbine blade, the number of material stations can be large. Further, the values of those material properties can vary dramatically from station to station. As such, an increase in the element order p could instigate a dramatically different solution, because the quadrature points may capture different material properties.

Pursuant to the DOE Public Access Plan, this document represents the authors' peer-reviewed, accepted manuscript.
The published version of the article is available from the relevant publisher.

For trapezoidal-rule quadrature, BeamDyn requires that the number of quadrature points be tied to the number of material stations and that, at a minimum, there is a quadrature point associated with each station; additional quadrature points (if desired) are equally distributed between those stations. Under this structure, $n_q = n_s + (n_s - 1) \times (j - 1) = (n_s - 1) \times j + 1$, where j is a positive integer that is user specified. Trapezoidal-rule quadrature enables a user to model a modern turbine blade defined by many cross-sectional property stations with few node points (i.e., $p \ll n_s$) while capturing all of the provided material properties. For example, the widely used NREL 5-MW reference wind turbine[40] blade is defined by 49 stations along the blade axis. If one were using first-order finite elements with a fixed quadrature scheme, at least 48 elements would be required to accurately capture the material data in the finite-element inner products. BeamDyn, with the GEBT model and LSFE p-type discretization, is equipped to model a wind turbine blade with a single element. LSFE discretization with trapezoidal-rule quadrature is an effective modeling approach when the beam deformation can be described accurately with relatively few finite-element nodes, despite the large number of material-property stations. However, for a given element order and $n_q \gg p$, solutions will be more expensive than if $n_q \approx p$ because inner products are evaluated at least once per time step.

2.4. Time integration and nonlinear-solution-stopping criterion

BeamDyn time integration is performed using the generalized-α scheme, which is an unconditionally stable (for linear systems), second-order-accurate algorithm. The scheme allows for users to choose integration parameters that introduce high-frequency numerical dissipation. More details regarding the generalized-α method can be found in Bauchau[38] and Chung and Hulbert.[41] Generalized-α time integration of the system defined by equations (1) and (2) [with linearized form in equation (9)] requires a nonlinear system solve at each time step.

The nonlinear-system solve is accomplished with the Newton–Raphson method, for which an energy-like stopping criterion has been chosen, which is calculated as

$$\| \Delta \mathbf{U}^{(i)T} \left({}^{t+\Delta t}\mathbf{R} - {}^{t+\Delta t}\mathbf{F}^{(i-1)} \right) \| \leq \| \epsilon_E \left(\Delta \mathbf{U}^{(1)T} \left({}^{t+\Delta t}\mathbf{R} - {}^{t}\mathbf{F} \right) \right) \| \tag{37}$$

where $\| \cdot \|$ denotes the Euclidean norm, $\Delta \mathbf{U}$ is the incremental displacement vector, $\mathbf{R}$ is the vector of externally applied nodal point loads, $\mathbf{F}$ is the vector of nodal point forces corresponding to the internal element stresses and ϵ_E is the preset energy tolerance. The superscript on the left side of a variable denotes the time value (in a dynamic analysis), whereas the one on the right side denotes the Newton–Raphson iteration number. As pointed out by Bathe and Cimento,[42] this criterion provides a measure of when the displacements and forces are near their equilibrium values.

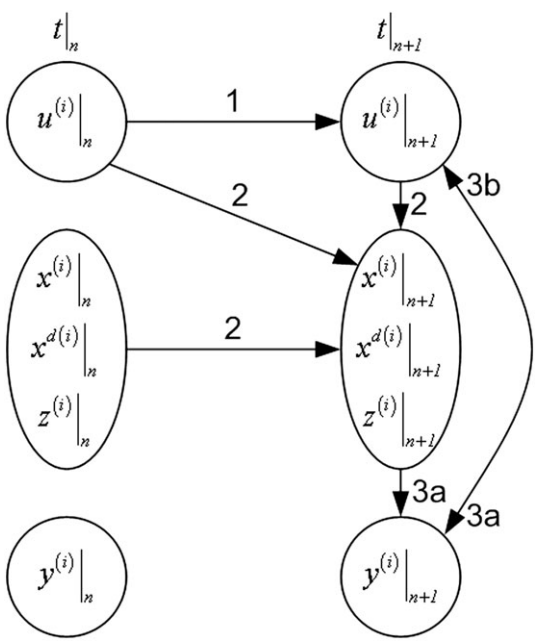

Figure 3. Module coupling algorithm for time marching in the FAST modularization framework.

Pursuant to the DOE Public Access Plan, this document represents the authors' peer-reviewed, accepted manuscript.
The published version of the article is available from the relevant publisher.

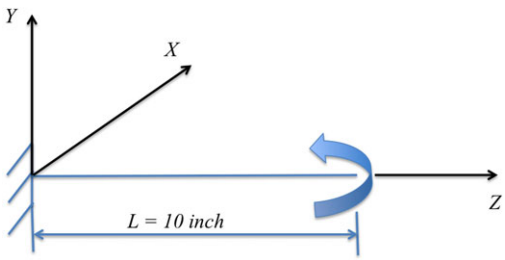

Figure 4. Schematic of a cantilever beam with tip moment, which was used in BeamDyn verification and performance studies. [Colour figure can be viewed at wileyonlinelibrary.com]

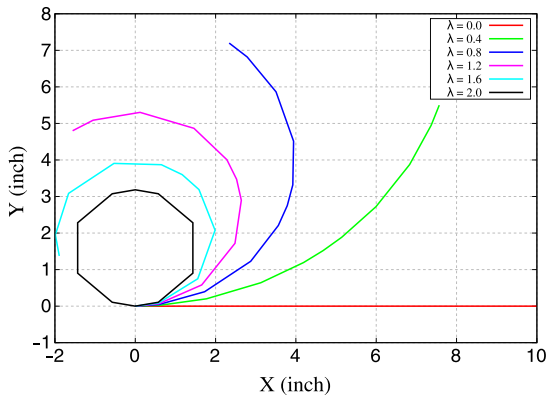

Figure 5. Static deflection of a cantilever beam (with straight lines connecting nodal solutions) under six constant bending moments as calculated with two fifth-order Legendre spectral FEs in BeamDyn. [Colour figure can be viewed at wileyonlinelibrary.com]

Table I. Comparison of analytical and BeamDyn-calculated tip displacements in the *Z* and *Y* directions (in inches) of a cantilever beam subjected to a constant moment; the BeamDyn model was composed of two fifth-order LSFEs.

λ	Analytical (*Z*)	BeamDyn (*Z*)	Analytical (*Y*)	BeamDyn (*Y*)
0.4	−2.4317	−2.4317	5.4987	5.4987
0.8	−7.6613	−7.6613	7.1978	7.1979
1.2	−11.5591	−11.5591	4.7986	4.7986
1.6	−11.8921	−11.8921	1.3747	1.3747
2.0	−10.0000	−10.0000	0.0000	0.0000

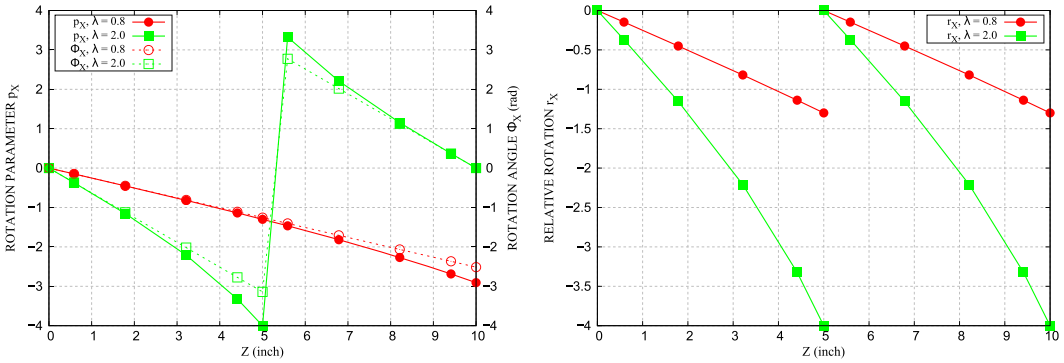

(a) Rotation parameter p_X and rotation angle ϕ_X **(b)** Relative rotation r_X

Figure 6. (a) Wiener–Milenković rotation parameters and rotation angles along the beam axis *Z* as calculated by BeamDyn for two tip moments; (b) relative rotations in the two elements. [Colour figure can be viewed at wileyonlinelibrary.com]

Pursuant to the DOE Public Access Plan, this document represents the authors' peer-reviewed, accepted manuscript. The published version of the article is available from the relevant publisher.

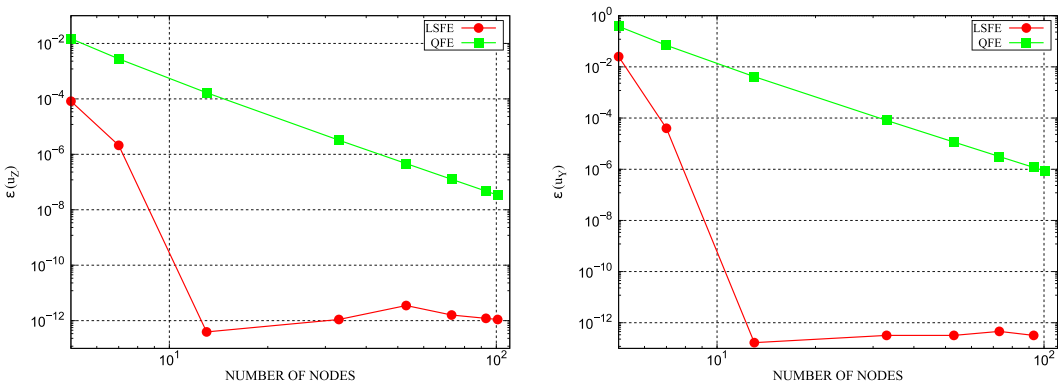

(a) u_Z **(b)** u_Y

Figure 7. Normalized error of the (a) u_Z and (b) u_Y tip displacements of a cantilever beam (Figure 4) under constant tip moment ($\lambda = 1.0$) as a function of the total number of nodes. Results were calculated with BeamDyn (LSFE) and Dymore (QFE). LSFE-model refinement was accomplished by increasing element polynomial order and QFE-model refinement was accomplished by increasing the number of elements. [Colour figure can be viewed at wileyonlinelibrary.com]

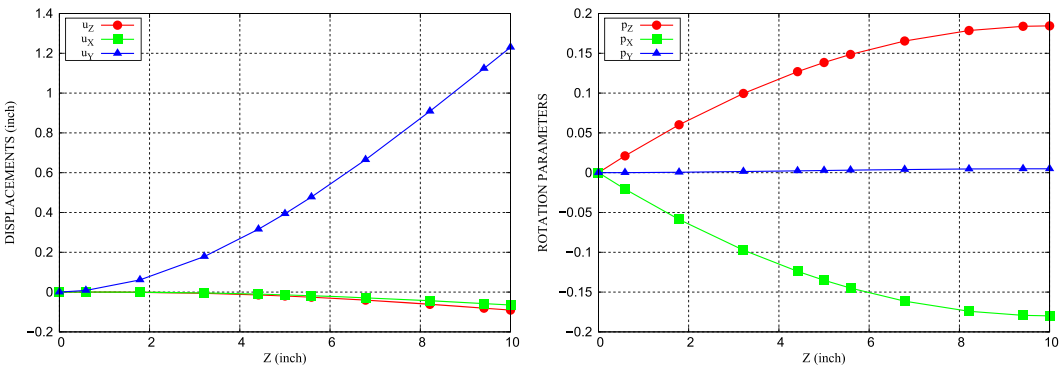

(a) Displacements **(b)** Rotations

Figure 8. Displacements and rotation parameters along the beam axis for example 2. [Colour figure can be viewed at wileyonlinelibrary.com]

2.5. Module coupling algorithm

The FAST modularization framework[30,43,44] was created to loosely couple multiphysics modules for time-domain simulation. Each module's internal variables are described by parameters (as constants) and states that are either continuous-in-time, discrete-in-time, constraints, or 'other' (e.g., logicals). Modules interact through input–output relationships, where output quantities are derived from inputs and states, and where inputs and outputs are defined on spatial meshes, and a predictor–corrector algorithm is employed to improve stability and accuracy of the time update of the coupled system. The modularization environment provides utilities for coupling nonmatching meshes in space and time. A detailed description of the coupling algorithm employed here can be found in Sprague *et al.*,[44] which we summarize here for the simplified case in which each module is advanced with the same time increment Δt, and where we ignore details regarding the mapping of information between modules with nonmatching meshes. Assume that we know all states, inputs and outputs at time t. In order to advance the states of all modules from time t to $t + \Delta t$, the following steps must be performed, which are illustrated in Figure 3.

(1) Using linear or quadratic extrapolation of known inputs, approximate the inputs at $t + \Delta t$.
(2) Update the states of all modules to $t + \Delta t$.
(3) Solve the global system of input–output equations at $t + \Delta t$. Depending on the relationship between modules and the module output equations, this system solve can range from a simple transfer of information to a full nonlinear-system solve.
(4) Either accept the states, inputs and outputs or apply a correction by repeating step 2 with the inputs calculated in step 3, and then repeating step 3.

Pursuant to the DOE Public Access Plan, this document represents the authors' peer-reviewed, accepted manuscript. The published version of the article is available from the relevant publisher.

Table II. Numerically determined tip displacements and rotation parameters of a composite beam in example 2 as calculated by BeamDyn (LSFE) and Dymore (QFE).

	u_Z (inch)	u_X(inch)	u_Y(inch)	p_Z	p_X	p_Y
BeamDyn	−0.09064	−0.06484	1.22998	0.18445	−0.17985	0.00488
Dymore	−0.09064	−0.06483	1.22999	0.18443	−0.17985	0.00488

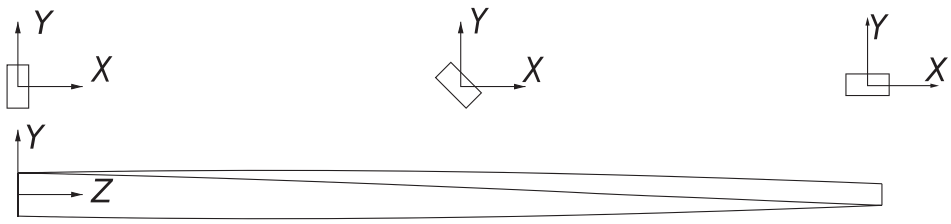

Figure 9. Sketch of the twisted beam.

Table III. Properties of the twisted beam.

Property	Value
Elastic Modulus	200 GPa
Shear Modulus	79.3 GPa
Height	0.5 m
Base	0.25 m
Length	10 m
Force	4000 kN

Table IV. Comparison of tip displacements of the twisted beam under a tip force.

	u_Z (m)	u_X (m)	u_Y (m)
BeamDyn	−1.132727	−1.715123	−3.578671
ANSYS	−1.134192	−1.714467	−3.584232
Percent difference	0.129	0.038	0.155

Sprague *et al.*,[43,44] showed, using simple numerical examples, that employing one or more correction steps can increase the accuracy of the coupled simulation as well as stability by permitting the use of larger time increments. However, these improvements in accuracy and stability must be weighed against the cost of additional 'update state' and 'output' calculations for each module.

3. NUMERICAL EXAMPLES

3.1. Example 1: static bending of a cantilever beam

The first example is a common benchmark problem for geometrically nonlinear analysis of beams.[2,45] We calculate the static deflection of a cantilever beam that is subjected at its free end to a constant moment about the negative X axis, M_X; a system schematic is shown in Figure 4. The length of the beam L is 10 inches, and the cross-sectional stiffness matrix is

$$C^* = 10^3 \times \begin{bmatrix} 1770 & 0 & 0 & 0 & 0 & 0 \\ 0 & 1770 & 0 & 0 & 0 & 0 \\ 0 & 0 & 1770 & 0 & 0 & 0 \\ 0 & 0 & 0 & 86.9 & 0 & 0 \\ 0 & 0 & 0 & 0 & 215 & 0 \\ 0 & 0 & 0 & 0 & 0 & 8.16 \end{bmatrix} \tag{38}$$

which has units of C^*_{ij} (lb), $C^*_{i,j+3}$ (lb·in) and $C^*_{i+3,j+3}$ (lb·in^2) for $i, j = 1, 2, 3$; these units are adopted for consistency

Pursuant to the DOE Public Access Plan, this document represents the authors' peer-reviewed, accepted manuscript.
The published version of the article is available from the relevant publisher.

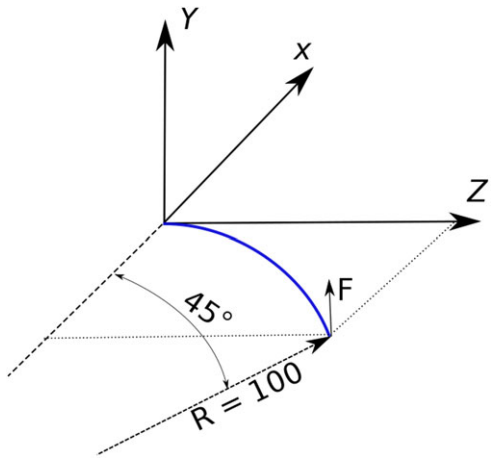

Figure 10. Sketch of the curved beam. [Colour figure can be viewed at wileyonlinelibrary.com]

Table V. Comparison of tip displacements of a curved beam under a tip force.

	Z (inches)	X (inches)	Y (inches)
BeamDyn (one LSFE)	−23.7	13.5	53.4
Bathe and Bolourchi[48]	−23.5	13.4	53.4

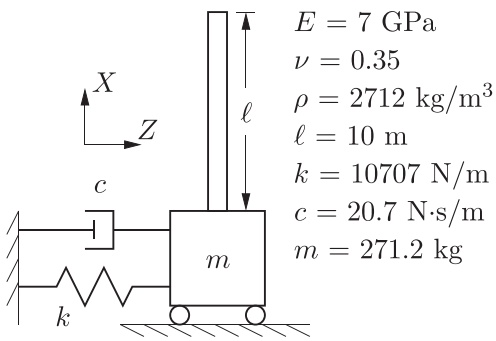

Figure 11. Schematic showing a beam clamped to a spring-damper-mass system with system properties and dimensions. The beam square cross section is 0.1 m × 0.1 m.

with those used in Yu *et al.*[13] and apply to example 2 as well. We note that the term with an asterisk denotes that it is resolved in the material basis and the sectional stiffness matrix $\underline{\underline{\mathcal{C}}}$ resolved in the inertial basis can be obtained by $\underline{\underline{\mathcal{C}}} = (\underline{\underline{R}}\,\underline{\underline{R}}_0)\underline{\underline{C}}^*(\underline{\underline{R}}\,\underline{\underline{R}}_0)^T$, where $\underline{\underline{R}}$ and $\underline{\underline{R}}_0$ denote the rotation matrix and the corresponding initial rotation matrix, respectively.

The load applied at the tip about the negative X direction is given by

$$M_X = \lambda \bar{M}_X \tag{39}$$

where $\bar{M}_X = \pi \frac{EI_X}{L}$ and $0 \leq \lambda \leq 2$ is a parameter used in the analytical solution. For $\lambda = 2$, the beam is bent into a full circle. In our simulations, the beam is discretized with two equal-length fifth-order LSFEs. We note that the maximum relative rotation in a single element cannot be greater than π as described in Bauchau *et al.*[39] in the current parameterization of 3-D rotations, which is why two elements are needed. The static deformations of the beam obtained from BeamDyn are shown in Figure 5 for six different tip moments. The calculated tip displacements are compared with the analytical solution in Table I, which were taken from Mayo *et al.*[46] as

Pursuant to the DOE Public Access Plan, this document represents the authors' peer-reviewed, accepted manuscript. The published version of the article is available from the relevant publisher.

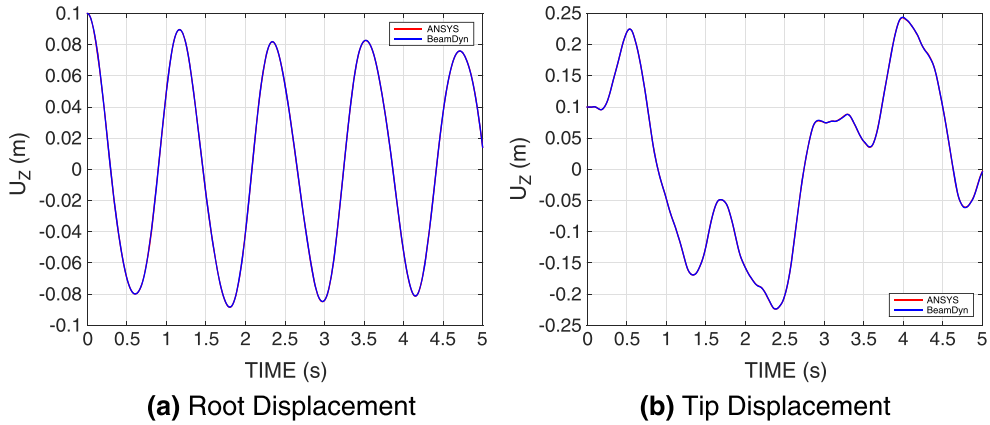

Figure 12. Beam-root and -tip horizontal-displacement histories calculated with ANSYS and BeamDyn for the beam-SDM system (Figure 11). The ANSYS and BeamDyn models were both time integrated with $\Delta t = 10^{-5}$ s. The ANSYS model had 60 BEAM188 elements, and the BeamDyn model had a single eighth-order element. [Colour figure can be viewed at wileyonlinelibrary.com]

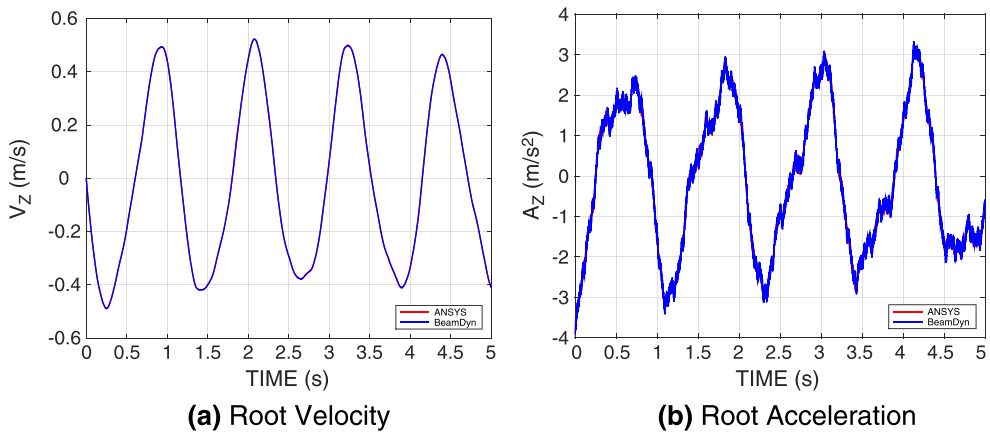

Figure 13. Beam-root horizontal velocity and acceleration histories calculated with ANSYS and BeamDyn for the beam-SDM system (Figure 11). Both models were time integrated with $\Delta t = 10^{-5}$ s. The ANSYS model had 60 BEAM188 elements, and the BeamDyn model had a single eighth-order element. [Colour figure can be viewed at wileyonlinelibrary.com]

$$u_Z = \rho \sin\left(\frac{Z}{\rho}\right) - Z \quad u_Y = \rho\left(1 - \cos\left(\frac{Z}{\rho}\right)\right) \tag{40}$$

where $\rho = \frac{EI_X}{M_X}$. At this discretization level, BeamDyn results are virtually identical to those of the analytical solution.

The rotation parameter p_X and rotation angle ϕ_X at each node along the beam axis Z obtained from BeamDyn are plotted in Figure 6(a) for $\lambda = 0.8$ and $\lambda = 2.0$. A rescaling can be observed in this figure for the case where $\lambda = 2.0$. Although the rotation parameters are not continuous between elements due to the rescaling operation, the relative rotations are continuous in a single element as described in Section 2.1, which can be observed in Figure 6(b).

Finally, we examine the accuracy of BeamDyn LSFEs as a function of model size. The accuracy convergence rate is compared with that of conventional quadratic elements used in Dymore,[47] which is a well known, finite-element-based, multibody dynamics code for the comprehensive modeling of flexible multibody systems. For each test case, BeamDyn and Dymore have approximately the same number of Newton–Raphson iterations. Figure 7 shows the normalized error $\varepsilon(u)$, where u is the calculated tip displacement (at $x = L$), as a function of the number of model nodes for the calculation with quadratic finite elements in Dymore and a single LSFE in BeamDyn, where

$$\varepsilon(u) = \left|\frac{u - u^a}{u^a}\right| \tag{41}$$

Pursuant to the DOE Public Access Plan, this document represents the authors' peer-reviewed, accepted manuscript.
The published version of the article is available from the relevant publisher.

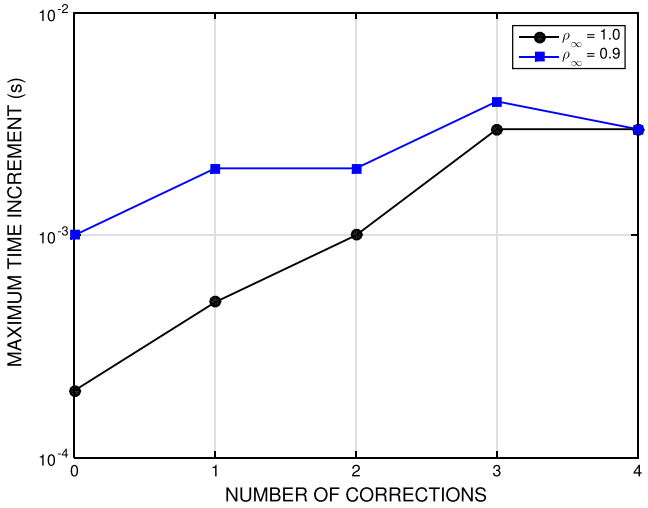

Figure 14. Maximum stable time increments as a function of the number of correction iterations in the predictor–corrector coupling algorithm for the BeamDyn-SDM system. Results are shown with ($\rho_\infty = 0.9$) and without ($\rho_\infty = 1.0$) numerical damping in the BeamDyn module. [Colour figure can be viewed at wileyonlinelibrary.com]

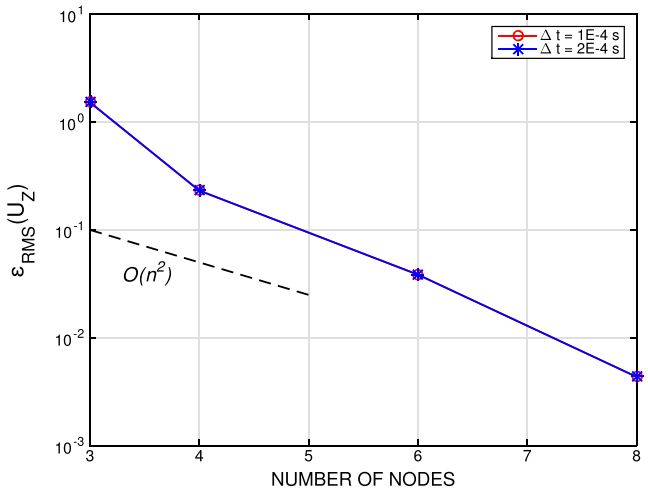

Figure 15. Normalized RMS error of horizontal tip-displacement histories as a function of total number of nodes for three different time increments. The dashed line shows ideal second-order convergence. The benchmark solution was calculated with a 9-node LSFE and $\Delta t = 5 \times 10^{-6}$ s. [Colour figure can be viewed at wileyonlinelibrary.com]

Table VI. RMS errors of tip-displacement histories for the BeamDyn-SDM system for several combinations of time increments and number of corrections in the loose-coupling algorithm.

Δt (s)	Number of corrections	ε_{RMS}
2×10^{-4}	0	3.85×10^{-2}
5×10^{-4}	1	5.78×10^{-2}
1×10^{-3}	2	3.85×10^{-2}
3×10^{-3}	3	3.83×10^{-2}
3×10^{-3}	4	3.82×10^{-2}

Results are shown for a BeamDyn model with 6 nodes and no numerical damping.

Pursuant to the DOE Public Access Plan, this document represents the authors' peer-reviewed, accepted manuscript. The published version of the article is available from the relevant publisher.

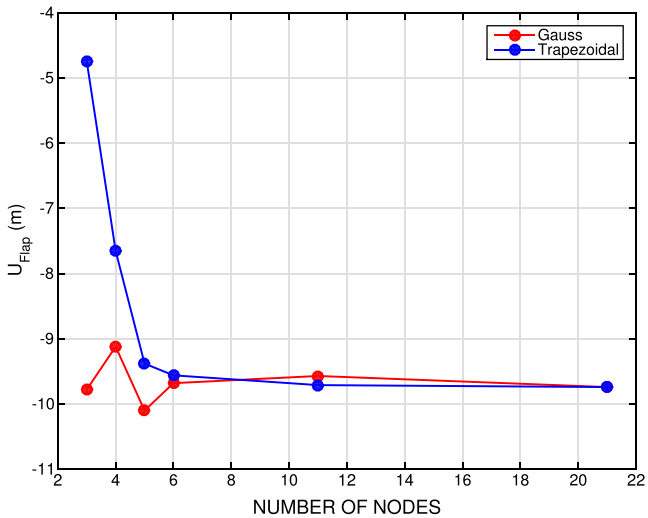

Figure 16. Tip deflections of a cantilevered NREL 5-MW blade under a uniformly distributed load as a function of the number of nodes in a single-element BeamDyn model where finite-element inner products were calculated with Gauss–Legendre or trapezoidal-rule quadrature. [Colour figure can be viewed at wileyonlinelibrary.com]

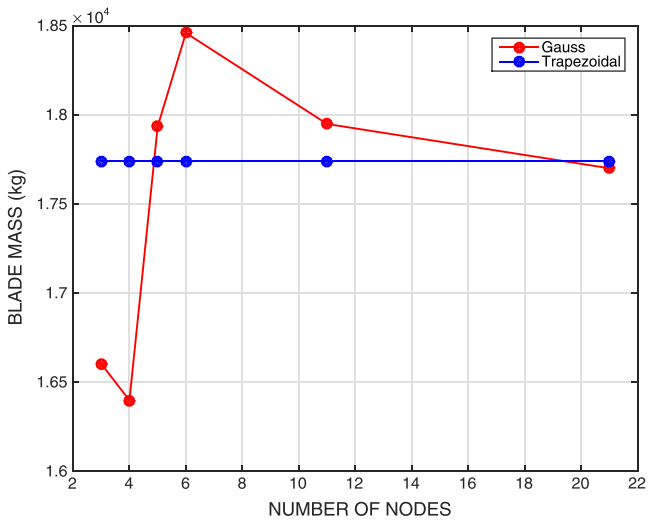

Figure 17. Total blade mass of an NREL 5-MW reference blade as a function of the number of nodes in a single-element BeamDyn model where finite-element inner products were calculated with Gauss–Legendre or trapezoidal-rule quadrature. [Colour figure can be viewed at wileyonlinelibrary.com]

and where u^a is the analytical solution. The parameter λ is set to 1.0 for this case. The LSFEs (with p-refinement) exhibit highly desirable exponential convergence to machine-precision error, whereas the conventional quadratic elements are limited to algebraic convergence. Here, for a given model size, an LSFE model can be orders of magnitude more accurate than its quadratic finite element counterpart.

3.2. Example 2: static analysis of a composite beam

The second example considers a composite beam with elastic coupling. The cantilever beam is 10 inches long with a boxed cross section made of composite materials that are defined in Yu *et al.*[13] Figure 4 shows a schematic of the cantilever beam.

Pursuant to the DOE Public Access Plan, this document represents the authors' peer-reviewed, accepted manuscript.
The published version of the article is available from the relevant publisher.

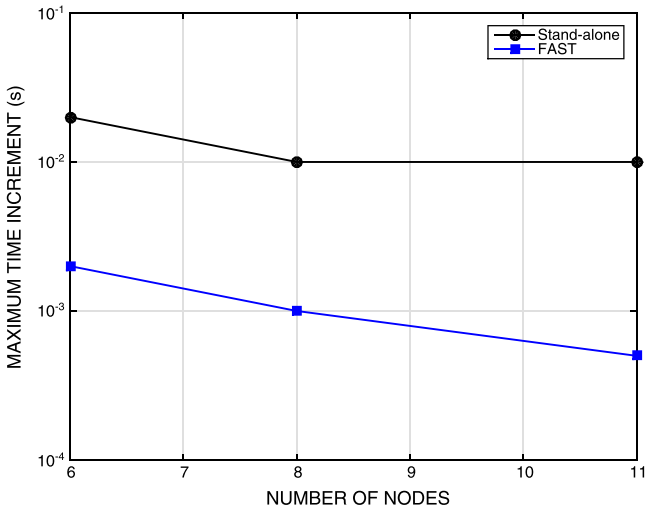

Figure 18. Maximum stable time increments versus number of FE nodes for an NREL 5-MW blade, wherein the blade is modeled with a single element. [Colour figure can be viewed at wileyonlinelibrary.com]

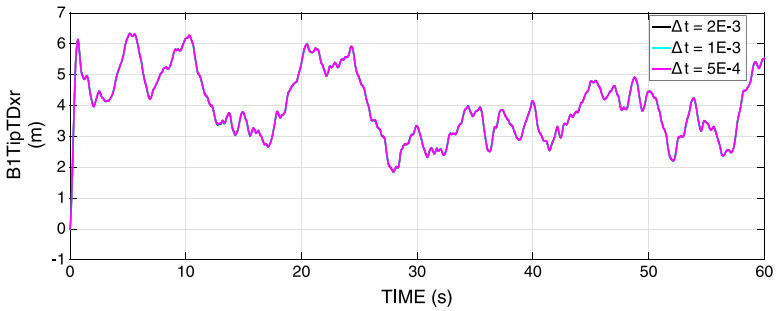

Figure 19. Blade tip deflection histories along flap direction obtained using different time increments, wherein the blade is modeled with a single fifth-order element. [Colour figure can be viewed at wileyonlinelibrary.com]

The stiffness matrix is given as

$$C^* = 10^3 \times \begin{bmatrix} 88.56 & 0 & 0 & 0 & 0 & 0 \\ 0 & 38.78 & 0 & 0 & 0 & 0 \\ 0 & 0 & 1368.17 & 0 & 0 & 0 \\ 0 & 0 & 0 & 59.12 & -0.370 & 17.61 \\ 0 & 0 & 0 & -0.370 & 141.47 & -0.351 \\ 0 & 0 & 0 & 17.61 & -0.351 & 16.96 \end{bmatrix} \tag{42}$$

A concentrated dead force $P_Y = 150$ lbs along the Y direction is applied at the free tip. In the BeamDyn analysis, the beam is meshed with two fifth-order elements. The displacements and rotation parameters at each node along the beam axis are plotted in Figure 8. We note that the coupling effects exist between the twist and two bending modes. The applied in-plane force leads to a fairly large twist angle due to the bend-twist coupling, which can be observed in Figure 8(b).

For verification, the tip displacements and rotations are compared with those obtained by a Dymore simulation in Table II, where the beam was meshed with 10 third-order elements. Good agreement can be observed between the BeamDyn and Dymore results.

3.3. Example 3: twisted and curved beams

We examine here beams that are twisted or curved in their undeformed configurations. We consider the twisted beam first. A straight beam ($k_X = k_Y = 0$) with an initial twist ($k_Z \neq 0$) is shown in Figure 9. The beam is linearly twisted in the

Pursuant to the DOE Public Access Plan, this document represents the authors' peer-reviewed, accepted manuscript. The published version of the article is available from the relevant publisher.

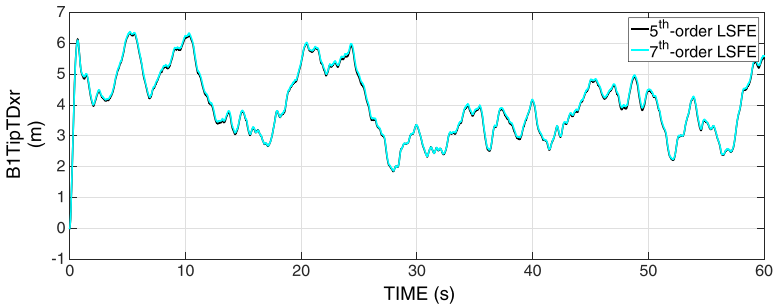

Figure 20. Blade tip deflection histories along flap direction obtained using different BeamDyn refinements, wherein models were time integrated with $\Delta t = 2 \times 10^{-3}$ s. [Colour figure can be viewed at wileyonlinelibrary.com]

positive θ_Z direction from 0 degrees at the root to 90 degrees at the tip. Table III shows the material properties for A36 steel, the beam geometry and the force applied at the free tip along the Y direction. The height and base values reported in the table are the height and base of the rectangular cross section. The beam was discretized using a seventh-order LSFE to obtain grid-independent results. The results for the twisted beam are shown in Table IV and are compared with the results obtained from an extremely refined 3-D ANSYS® finite-element analysis using 84,000 SOLID186 elements. We see that the tip results are quite large (35% of total length) and that the agreement between the solid-element and beam-element solutions is very good. These results also serve to validate the beam-modeling approach.

Next, a curved beam was examined. It is clear that the curvature plays a major role in the distribution of the elastic forces within the beam. As such, it is very important to ensure that BeamDyn is capable of modeling this effect properly. A widely used benchmark problem for a curved beam is the case proposed by Bathe and Bolourchi,[48] which was chosen for verification. Figure 10 shows the configuration of the cantilevered curved beam being analysed. The beam lies in the X, Z plane, in the quadrant defined by positive Z and negative X directions. The beam is defined by a 45-degree arc with a 100-inch radius centered at $X = -100$ inches and $Z = 0$ inches. The geometry of the cross section for the curved beam is square, and the material properties can be found in Bathe and Bolourchi.[48] A force of 600 pounds was applied in the positive Y direction. The beam was discretized by a single fifth-order LSFE. The results of the static analysis are shown in Table V and are compared with the results published in Bathe and Balourchi.[48] Excellent agreement is demonstrated.

3.4. Example 4: partitioned analysis

In this example, we have an oversimplified representation of a turbine blade connected to a hub, where a beam is 'clamped' to the mass in a spring-damper-mass (SDM) system as shown in Figure 11; except for the horizontal motion, the other five degrees of freedom at the beam's base are constrained to zero. We use this example to verify our numerical implementation and to examine the accuracy and numerical behavior of the multibody coupling algorithm. In this configuration, the relevant output from BeamDyn, in terms of the coupling algorithm, is translation reaction force, whereas its inputs are root motion (translational displacement, velocity and acceleration). The inputs and outputs are the same, but swapped, for the SDM system. As described previously, the time integrator in BeamDyn is a second-order implicit generalized-alpha algorithm, and the time integrator for the SDM system is the fourth-order Adams–Bashforth–Moulton method, which is a predictor–corrector algorithm. The material properties, coordinate system and geometric parameters can be found in Figure 11, where E, ν, ρ and ℓ are the beam's elastic modulus, Poisson ratio, density and length, respectively. The square cross-sectional dimensions of the beam are 0.1 m × 0.1 m. The natural frequency of the uncoupled mass-spring-damper system is 6.28 rad/s, and the first five distinct natural frequencies for the uncoupled beam (in a clamped/cantilevered configuration) are 0.26, 1.72, 5.78, 22.62 and 24.21 rad/s, respectively, as determined by a refined ANSYS Mechanical modal analysis. The first five distinct natural frequencies of the coupled system, obtained by ANSYS modal analysis, are 0.25, 0.85, 1.80, 4.76 and 9.34 rad/s, respectively.

For verification, we analysed the system in ANSYS using 60 BEAM188 elements cantilevered to a point mass with spring and damper elements, and the time increment was 10^{-5} s. The Newmark-β time integrator was employed in ANSYS without numerical damping. For the BeamDyn results, the beam was discretized by a single eighth-order element, and the time increment was 10^{-5} s. BeamDyn inner products were evaluated with standard Gauss–Legendre quadrature. Unless otherwise noted, BeamDyn numerical damping was disabled, and there was no correction step in the coupling algorithm. Second-order extrapolation and interpolation in the coupling algorithm were employed. Simulations were performed with quiescent initial conditions, but with the mass and beam initially displaced 0.1 m in the Z direction. The root and tip

Pursuant to the DOE Public Access Plan, this document represents the authors' peer-reviewed, accepted manuscript.
The published version of the article is available from the relevant publisher.

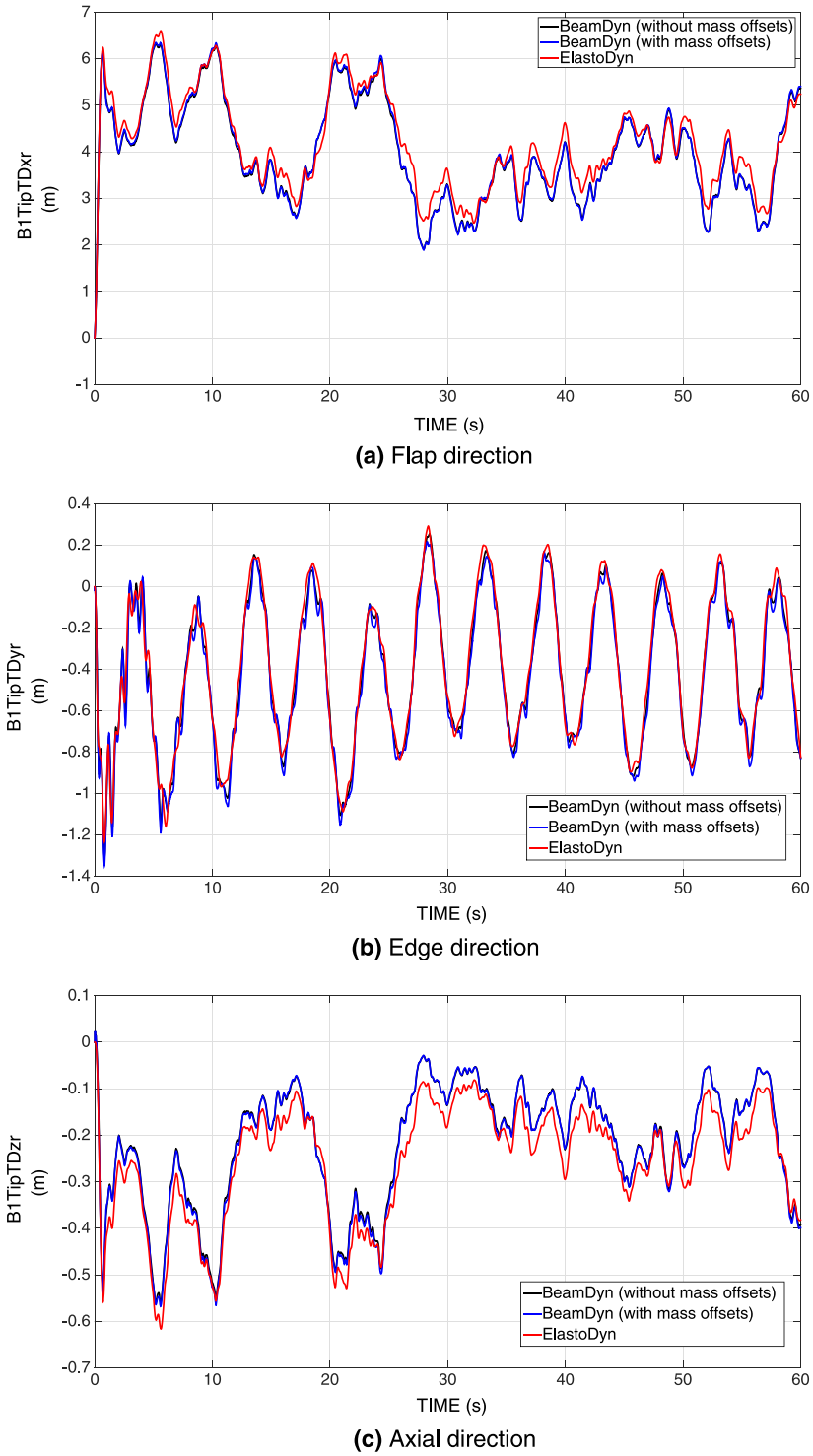

Figure 21. Comparisons of blade tip displacements between ElastoDyn and BeamDyn results. [Colour figure can be viewed at wileyonlinelibrary.com]

Pursuant to the DOE Public Access Plan, this document represents the authors' peer-reviewed, accepted manuscript. The published version of the article is available from the relevant publisher.

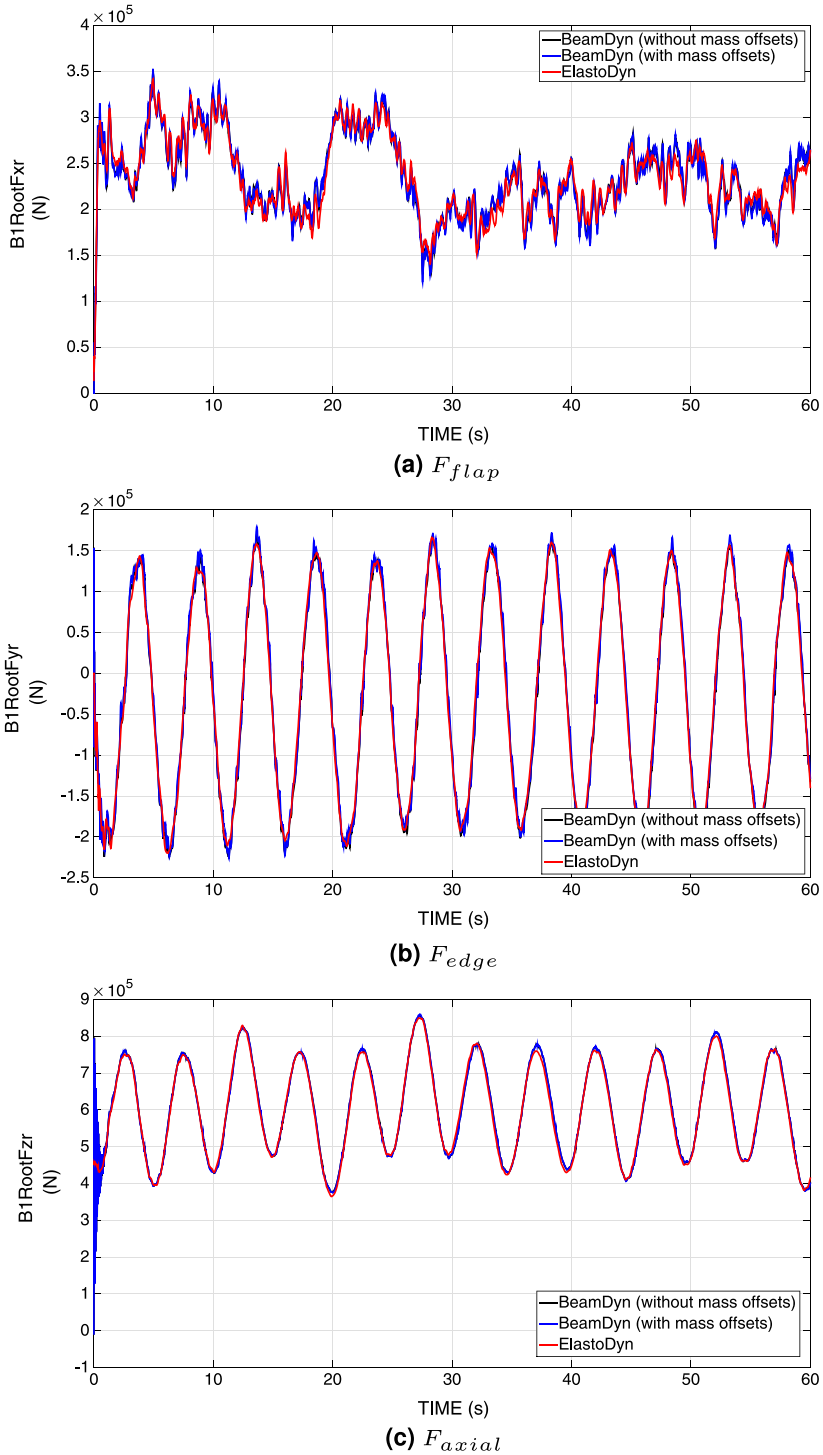

Figure 22. Comparisons of root reaction forces between ElastoDyn and BeamDyn results. [Colour figure can be viewed at wileyonlinelibrary.com]

Pursuant to the DOE Public Access Plan, this document represents the authors' peer-reviewed, accepted manuscript. The published version of the article is available from the relevant publisher.

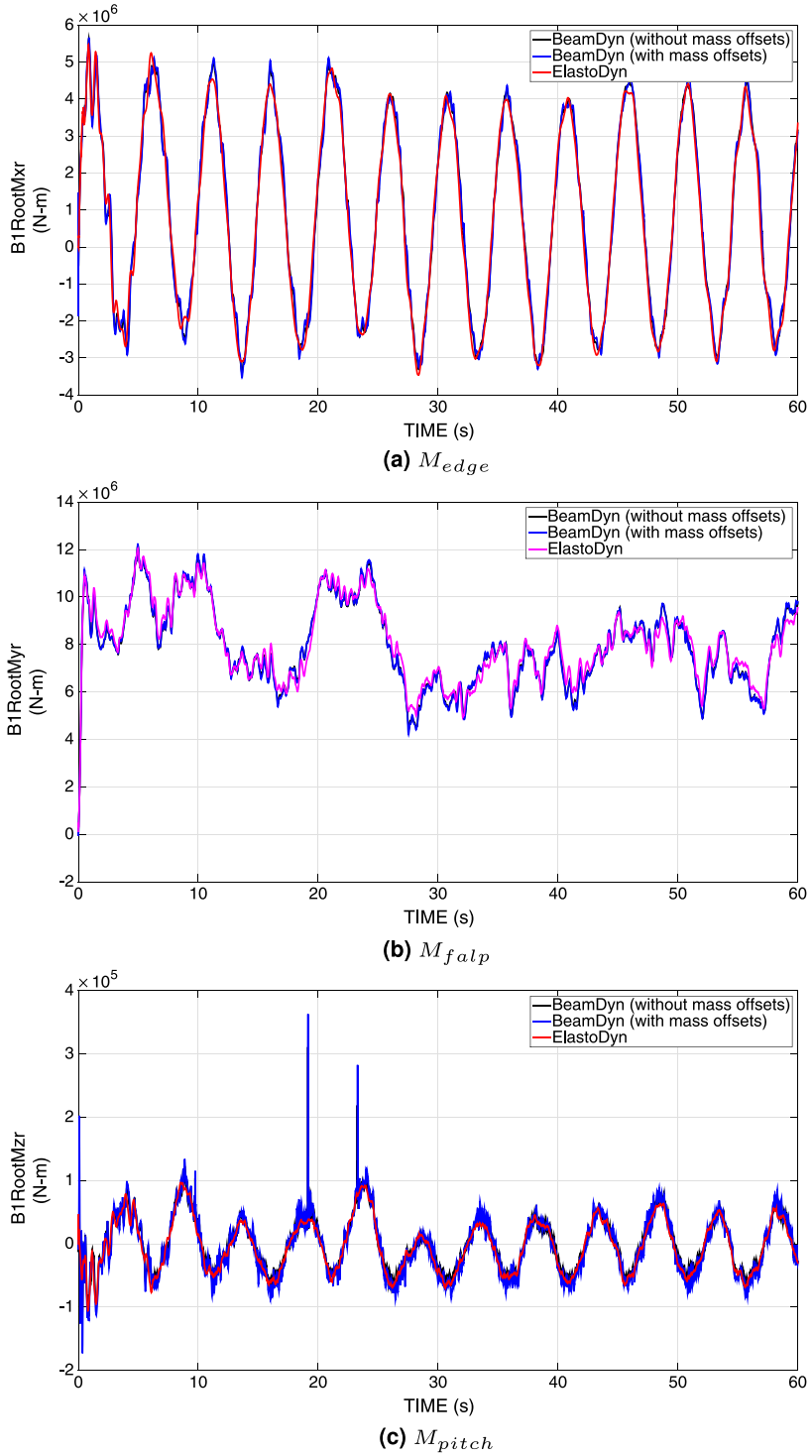

Figure 23. Comparisons of root reaction moments between ElastoDyn and BeamDyn results. [Colour figure can be viewed at wileyonlinelibrary.com]

Pursuant to the DOE Public Access Plan, this document represents the authors' peer-reviewed, accepted manuscript. The published version of the article is available from the relevant publisher.

displacements of the beam calculated with the two models are shown in Figure 12. Excellent agreement is demonstrated between the ANSYS and BeamDyn results. The root horizontal velocity and acceleration are also compared between the two models in Figure 13. Again, excellent agreement is shown.

For the BeamDyn-SDM system, we consider first the stability of the coupling algorithm for which the beam is discretized by a single fifth-order LSFE. Figure 14 shows the maximum stable time increments for the BeamDyn-SDM system, obtained by numerical experiments, against the number of correction iterations in the FAST loose-coupling scheme; the predictor–corrector algorithm was presented in Section 2.5. Results are shown with and without numerical damping in the BeamDyn module. Increasing the number of correction iterations, up to three iterations, increases the allowable time increment for stability. In moving from three to four corrections, however, we see no increase in stability for the numerical-damping-free simulations, and we even see a small decrease in stability with BeamDyn numerical damping. Overall, however, the inclusion of numerical damping in BeamDyn increases the allowable time increment for stable solutions. The computational savings offered by a larger stable time increment provided by additional correction steps must be considered against the additional computational cost of the correction steps. For example, adding a single correction step makes each time step about twice as expensive compared with no correction. We also note that the maximum stable time increment for the uncoupled BeamDyn model (without numerical damping) is 5×10^{-3} s. Thus, the coupled system is more stiff.

We consider here the accuracy of the coupled model for the BeamDyn-SDM system by examining solutions calculated with various spatial and temporal discretization levels. Accuracy was quantified by root-mean-square (RMS) error, ε_{RMS}, which was calculated as

$$\varepsilon_{RMS} = \sqrt{\frac{\sum_{k=0}^{n_{max}} [U_z^k - U_b(t^k)]^2}{\sum_{k=0}^{n_{max}} [U_b(t^k)]^2}} \tag{43}$$

and where $U_b(t)$ is the benchmark solution calculated with a BeamDyn-SDM model with a 9-node beam model and $\Delta t = 5 \times 10^{-6}$ s. Figure 15 shows the RMS error of the horizontal tip displacements as a function of the total number of BeamDyn nodes for two different time increments (1×10^{-4} s and 2×10^{-4} s); BeamDyn had no numerical damping, and there were no correction steps in the loose-coupling algorithm. The results indicate that $\Delta t = 2 \times 10^{-4}$ s provides time-increment-independent solutions. We see approximately second-order convergence with spatial refinement (increase in the number of nodes), and results indicate that a fifth-order element (six nodes) provides results of good accuracy. Table VI shows RMS errors of tip-displacement histories for the BeamDyn-SDM system for several combinations of time increments and number of corrections in the loose-coupling algorithm. We see that, for this system, increasing the number of corrections permits larger time increments while maintaining sufficient accuracy.

3.5. Example 5: NREL 5-MW wind turbine

The last example is an analysis of the NREL 5-MW reference wind turbine,[40] which has straight, 61.5 m blades. We examine simulation results wherein the blades are modeled by BeamDyn or ElastoDyn. The blade structural-dynamics model in the ElastoDyn module of FAST can well be applied to straight isotropic blades dominated by bending. The ElastoDyn model includes two flapwise-bending deformation modes and one edgewise-bending deformation mode, coupled through a structural pre-twist, but neglects axial, shear and torsional degrees of freedom as well as mass and elastic offsets from the pitch axis. Several geometric and kinematic nonlinearities are accounted for, including radial shortening and centrifugal, Coriolis and gyroscopic loading.

We examine here the numerical performance of two different BeamDyn quadrature methods, Gauss–Legendre and trapezoidal rule, for this realistic-blade analysis. As described earlier, the sectional properties for the NREL 5-MW reference turbine blade are defined at 49 evenly spaced stations along its 61.5 m length. First, a cantilevered blade under a uniformly distributed static force of magnitude 10^4 N/m along the flap direction is analysed. Figure 16 shows the tip displacement in the flap direction as a function of the number of nodes. Monotonic convergence of tip displacement is shown for the trapezoidal-quadrature results with an increasing number of nodes. The convergence rate of tip displacements for Gauss–Legendre quadrature, however, is non-monotonic. As described in Section 2.3, the trapezoidal-rule quadrature captures all 49 material-data stations regardless of the number of element nodes, whereas the particular material data incorporated by Gauss–Legendre quadrature varies with the number of element nodes. The advantage of trapezoidal-rule quadrature is also demonstrated in the calculation of total blade mass as shown in Figure 17. The total blade mass as calculated with trapezoidal-rule quadrature is independent of the number of nodes, whereas the mass calculated by Gauss–Legendre quadrature depends on the number of nodes in the element, and a large number of nodes is required for an accurate total-mass calculation. We note that a small scaling factor has been applied to the calculation of blade mass with ElastoDyn and BeamDyn to ensure each is consistent with the target total mass. In all subsequent calculations with BeamDyn, trapezoidal-rule quadrature is employed.

Pursuant to the DOE Public Access Plan, this document represents the authors' peer-reviewed, accepted manuscript.
The published version of the article is available from the relevant publisher.

Next, we studied the time step sizes required for stable simulation of BeamDyn in stand-alone and coupled-to-FAST configurations. Figure 18 shows the maximum time step size versus the number of nodes for a BeamDyn model composed of a single element. In the stand-alone configuration, we used FAST as the driver but with all coupling options disabled so that the blade rotated at a fixed speed loaded only by gravity. For the coupled-to-FAST case, we conducted an aero-servo-elastic wind turbine analysis under a mean wind speed of 12 m/s with turbulence, which is certification test case #26 in the FAST archive.[49] BeamDyn numerical damping was disabled, and there were no correction iterations in the coupling algorithm. We see that the two-way coupling between BeamDyn and FAST requires significantly smaller time increments for stable solutions.

Finally, we studied the performance of BeamDyn in the coupled FAST analysis. Figures 19 and 20 show the tip flap displacement histories under different time and space discretizations. Note that all of the quantities studied here are defined in the body-attached blade reference coordinate system following the International Electrotechnical Commission standard, where the X direction is toward the suction side of the airfoil, the Y direction is toward the trailing edge and the Z direction is toward the blade tip from the root. These results demonstrate that, for this system, results that are grid independent (in space and time) can be obtained with $\Delta t = 2 \times 10^{-3}$ s and a single fifth-order element for each blade.

We compared the results obtained by BeamDyn with those obtained by ElastoDyn for the coupled analysis (as described earlier). The BeamDyn blades were each modeled with a single fifth-order element (6 nodes), and the FAST-BeamDyn system was time integrated with $\Delta t = 2 \times 10^{-3}$ s, which was required for numerical stability. The FAST-ElastoDyn system was time integrated with $\Delta t = 1.25 \times 10^{-2}$ s. The tip displacements of blade 1 are shown in Figure 21. Results for BeamDyn are shown with and without off-diagonal terms in the sectional mass matrices (the latter is for more direct comparison with ElastoDyn). Good agreement can be observed between the ElastoDyn and BeamDyn results. We note that, because of the trapeze effect and elastic stretching considered in BeamDyn, the mean value of the axial tip displacement calculated by BeamDyn is different than that calculated by ElastoDyn. Figures 22 and 23 show the root reaction forces and moments, respectively, calculated by BeamDyn and ElastoDyn. Again, good agreement is shown. We note the spurious spikes in the M_{pitch} histories, which will be addressed in a future release of BeamDyn. Although we see noticeable differences in the tip-displacement histories, it is interesting to note the excellent agreement between ElastoDyn and BeamDyn results for root reaction forces and moments. This is because the NREL 5-MW blade features are well modeled by the approximations behind the ElastoDyn model. In particular, ElastoDyn is well suited for modeling the NREL 5-MW blade because:

- the blade is naturally straight,
- the lowest modes excited by wind are dominated by bending,
- there are no cross-sectional couplings induced by anisotropic composite laminate layups,
- torsion, extension and shear effects are mostly negligible (the first torsional mode natural frequency is well above rated rotor speed; the blade aspect ratio is high, and so on),
- the deflections are small enough that they can be accurately captured by the geometric nonlinear terms included in ElastoDyn and
- the mass-center offsets are small and do not cause a large change in response.

The benefits of moving from an efficient lower-fidelity model like ElastoDyn to a more computationally expensive higher-fidelity model like BeamDyn will be best seen for turbine blades that do not satisfy the above simplifying features, e.g., those with aeroelastically tailored curved blades. For example, Guntur *et al.*[50] examined the simulated and field-measured responses of a Siemens 2.3 MW turbine with a 108-m rotor for 1141 cases with various wind speeds and turbulence intensities. The Siemens turbine had flexible aeroelastically tailored blades with bend-twist coupling. Simulations were performed with the blades modeled in both BeamDyn and ElastoDyn. The BeamDyn models gave results that agreed significantly better, and in some cases dramatically better, with the field measurements for nearly all quantities investigated.

4. CONCLUSION

This paper presents a displacement-based implementation of GEBT for three-dimensional nonlinear elastic deformation. LSFEs are adopted for spatial discretization of the beam. The open-source software module, BeamDyn, can be used either as a stand-alone beam solver or a structural dynamics module for wind turbine blade analysis in the FAST modularization framework. Numerical examples were presented that demonstrate and validate the capability of BeamDyn. A benchmark static problem for nonlinear deformation of a beam was studied first. The agreement between the results calculated by BeamDyn and the analytical solution is excellent. Moreover, an accuracy convergence study was conducted, wherein the convergence rate of Legendre spectral elements was compared with that of conventional quadratic finite elements. Exponential convergence rates were observed as expected. A composite beam and beams with curved and twisted undeformed configurations were studied, and the results were compared against those obtained by Dymore or ANSYS. The FAST module coupling algorithm and the performance of BeamDyn as a module in FAST were examined with two numerical examples. The features of BeamDyn can be summarized as follows:

Pursuant to the DOE Public Access Plan, this document represents the authors' peer-reviewed, accepted manuscript.
The published version of the article is available from the relevant publisher.

(1) On the basis of GEBT, BeamDyn is capable of dealing with geometric nonlinear beam problems with arbitrary magnitude of displacements and rotations for both static and dynamic analyses.
(2) Along with a preprocessor like PreComp or VABS, BeamDyn takes full elastic coupling effects into account.
(3) The spatial domain is discretized by Legendre spectral finite elements, which are p-type finite elements, so that exponential convergence rates can be expected for smooth solutions.
(4) BeamDyn is implemented following the programming requirements (data structures and interfaces) of the FAST modularization framework.

ACKNOWLEDGEMENTS

The submitted manuscript has been offered by employees of the Alliance for Sustainable Energy, LLC (Alliance), a contractor of the US Government under Contract No. DE-AC36-08GO28308. This work was supported by the US Department of Energy under contract no. DE-AC36-08GO28308 with the NREL. Funding for the work was provided by the DOE Office of Energy Efficiency and Renewable Energy, Wind and Water Power Technologies Office. The US Government retains, and the publisher, by accepting the paper for publication, acknowledges that the US Government retains a nonexclusive, paid-up, irrevocable, worldwide license to publish or reproduce the published form of this work, or allow others to do so, for US Government purposes. Support was also provided through a National Renewable Energy Laboratory Directed Research and Development Grant *High-Fidelity Computational Modeling of Wind-Turbine Structural Dynamics*. The authors thank the reviewers and Sheri Anstedt for helpful suggestions for improving the paper.

REFERENCES

1. Reissner E. On one-dimensional large-displacement finite-strain beam theory. *Studies in Applied Mathematics LII* 1973; **52**: 87–95.
2. Simo JC. A finite strain beam formulation. The three-dimensional dynamic problem. Part I. *Computer Methods in Applied Mechanics and Engineering* 1985; **49**: 55–70.
3. Simo JC, Vu-Quoc L. A three-dimensional finite-strain rod model. Part II. *Computer Methods in Applied Mechanics and Engineering* 1986; **58**: 79–116.
4. Jelenić G, Crisfield MA. Geometrically exact 3D beam theory: implementation of a strain-invariant finite element for statics and dynamics. *Computer Methods in Applied Mechanics and Engineering* 1999; **171**: 141–171.
5. Betsch P, Steinmann P. Frame-indifferent beam finite elements based upon the geometrically exact beam theory. *International Journal for Numerical Methods in Engineering* 2002; **54**: 1775–1788.
6. Ibrahimbegović A. On finite element implementation of geometrically nonlinear Reissner's beam theory: three-dimensional curved beam elements. *Computer Methods in Applied Mechanics and Engineering* 1995; **122**: 11–26.
7. Ibrahimbegović A, Mikdad MA. Finite rotations in dynamics of beams and implicit time-stepping schemes. *International Journal for Numerical Methods in Engineering* 1998; **41**: 781–814.
8. Hodges D. A mixed variational formulation based on exact intrinsic equations for dynamics of moving beams. *International Journal of Solids and Structures* 1990; **26**: 1253–1273.
9. Cook RD, Malkus DS, Plesha ME, Witt RJ. *Concepts and Applications of Finite Element Analysis* 4th ed. Wiley: New York, NY, 2001.
10. Yu W, Blair M. GEBT: a general-purpose nonlinear analysis tool for composite beams. *Composite Structures* 2012; **94**: 2677–2689.
11. Wang Q, Yu W, Sprague MA. Geometric nonlinear analysis of composite beams using Wiener-Milenković parameters. *Proceedings of the 54th Structures, Structural Dynamics, And Materials Conference*, Boston, Massachusetts, 2013; AIAA 2013–1697.
12. Bir GS, User's guide to PreComp (Pre-processor for computing composite beam properties), Technical Report NREL/TP-500-38929, National Renewable Energy Laboratory, Golden, CO, 2006.
13. Yu W, Hodges DH, Volovoi V, Cesnik CES. On Timoshenko-like modeling of initially curved and twisted composite beams. *International Journal of Solids and Structures* 2002; **39**: 5101–5121.
14. Blasques J, Bitsche R, Fedorov V, Lazarov B. Accuracy of an efficient framework for structural analysis of wind turbine blades. *Wind Energy* 2016; **19**: 1603–1621.
15. Berg J, Resor B, *Numerical manufacturing and design tool (NuMAD v2.0) for wind turbine blades: users guide*, Technical Report SAND2012-7028, Sandia National Laboratories, Albuquerque, NM, 2012.

Pursuant to the DOE Public Access Plan, this document represents the authors' peer-reviewed, accepted manuscript.
The published version of the article is available from the relevant publisher.

16. Hodges D, Yu W. A rigorous engineer-friendly approach for modeling realistic, composite rotor blades. *Wind Energy* 2007; **10**: 179–193.
17. Chen H, Yu W, Capellaro M. A critical assessment of computer tools for calculating composite wind turbine blade properties. *Wind Energy* 2010; **13**: 497–516.
18. Hodges DH. *Nonlinear Composite Beam Theory*. AIAA: Reston, VA, 2006.
19. Patera AT. A spectral element method for fluid dynamics: laminar flow in a channel expansion. *Journal of Computational Physics* 1984; **54**: 468–488.
20. Ronquist EM, Patera AT. A Legendre spectral element method for the Stefan problem. *International Journal for Numerical Methods in Engineering* 1987; **24**: 2273–2299.
21. Deville MO, Fischer PF, Mund EH. *High-order methods for incompressible fluid flow*. Cambridge University Press: New York, NY, 2002.
22. Komatitsch D, Vilotte JP. The spectral element method: an efficient tool to simulate the seismic response of 2D and 3D geological structures. *Bulletin of the Seismological Society of America* 1998; **88**: 368–392.
23. Sridhar R, Chakraborty A, Gopalakrishnan S. Wave propagation in anisotropic and inhomogeneous untracked and cracked structures using the pseudo spectral finite element method. *International Journal of Solids and Structures* 2006; **43**: 4997–5031.
24. Sprague MA, Geers TL. A spectral-element method for modeling cavitation in transient fluid–structure interaction. *International Journal for Numerical Methods in Engineering* 2004; **60**: 2467–2499.
25. Bar-Yoseph P, Fisher D, Gottlieb O. Spectral element methods for nonlinear spatio-temporal dynamics of an Euler-Bernoulli beam. *Computational Mechanics* 1996; **19**: 136–151.
26. Sprague MA, Geers TL. Legendre spectral finite elements for structural dynamics analysis. *Communications in Numerical Methods in Engineering* 2008; **24**: 1953–1965.
27. Zrahia U, Bar-Yoseph P. Plate spectral elements based upon Reissner–Mindlin theory. *International Journal for Numerical Methods in Engineering* 1995; **38**: 1341–1360.
28. Sprague MA, Brito KD. Reissner–Mindlin Legendre spectral finite elements with mixed reduced quadrature. *Finite Elements in Analysis and Design* 2012; **58**: 74–83.
29. Sprague MA, Purkayastha A. Legendre spectral finite elements for Reissner–Mindlin composite plates. *Finite Elements in Analysis and Design* 2015; **105**: 33–43.
30. Jonkman JM. The new modularization framework for the FAST wind turbine CAE tool. *Proceedings of the 51st AIAA Aerospace Sciences Meeting Including the New Horizons Forum and Aerospace Exposition*, Grapevine, Texas, 2013; AIAA 2013–0202.
31. Jonkman J, Jonkman B. FAST v8, 2013. https://nwtc.nrel.gov/FAST8 [Online; accessed 29-OCTOBER-2014].
32. Jonkman JM. Development of FAST.Farm: a new multi-physics engineering tool for wind-farm design and analysis. *Proceedings of AIAA Science and Technology Forum and Exhibition (SciTech 2017)*, Grapevine, Texas, 2017; AIAA 2017-0454. To appear.
33. Øye S. FLEX4 simulation of wind turbine dynamics. *28th IEA Meeting of Experts Concerning State of the Art of Aeroelastic Codes for Wind Turbine Calculations*, Lyngby, Denmark, 1996. Available through IEA.
34. Garrad Hassan and Partners Ltd. *Bladed theory manual v4.7*, 2015.
35. Kim T, Hansen A, Branner K. Development of an anisotropic beam finite element for composite wind turbine blades in multibody system. *Renewable Energy* 2013; **59**: 172–183.
36. Su W, Cesnik C. Strain-based geometrically nonlinear beam formulation for modeling very flexible aircraft. *International Journal of Solids and Structures* 2011; **48**: 2349–2360.
37. Su W, Song W. Nonlinear aeroelastic modeling and analysis of flexible wind turbine blades. *Proceedings of the 56th AIAA/ASCE/AHS/ASC Structures, Structural Dynamics, and Materials Conference*, Kissimmee, Florida, 2015.
38. Bauchau OA. *Flexible Multibody Dynamics*. Springer: New York, NY, 2010.
39. Bauchau O, Epple A, Heo S. Interpolation of finite rotations in flexible multibody dynamics simulations. *Proceedings of the Institution of Mechanical Engineers, Part K: Journal of Multi-body Dynamics* 2008; **222**: 353–366.
40. Jonkman J, Butterfield S, Musial W, Scott G, *Definition of a 5-MW reference wind turbine for offshore system development*, Technical Report NREL/TP-500-38060, National Renewable Energy Laboratory, Golden, CO, 2009.
41. Chung J, Hulbert GM. A time integration algorithm for structural dynamics with improved numerical dissipation: the generalized-α method. *Journal of Applied Mechanics* 1993; **60**: 371–375.
42. Bathe KJ, Cimento AP. Some practical procedures for the solution of nonlinear finite element equations. *Computer Methods in Applied Mechanics and Engineering* 1980; **22**: 59–85.

Pursuant to the DOE Public Access Plan, this document represents the authors' peer-reviewed, accepted manuscript.
The published version of the article is available from the relevant publisher.

43. Sprague M, Jonkman J, Jonkman B. FAST modular wind turbine CAE tool: non-matching spatial and temporal meshes. *Proceedings of the 32nd ASME Wind Energy Symposium*, National Harbor, Maryland, 2014; AIAA 2014–0520.
44. Sprague MA, Jonkman J, Jonkman B. FAST modular framework for wind turbine simulation: new algorithms and numerical examples. *Proceedings of the 33rd ASME Wind Energy Symposium*, Kissimmee, Florida, 2015; AIAA 2015–1461.
45. Xiao N, Zhong H. Non-linear quadrature element analysis of planar frames based on geometrically exact beam theory. *International Journal of Non-Linear Mechanics* 2012; **47**: 481–488.
46. Mayo JM, García-Vallejo D, Domínguez J. Study of the geometric stiffening effect: comparison of different formulations. *Multibody System Dynamics* 2004; **11**: 321–341.
47. Bauchau OA. Dymore user's manual, 2013. http://dymoresolutions.com/dymore4_0/UsersManual/UsersManual.html (Accessed 1 December 2013).
48. Bathe KJ, Bolourchi S. Large displacement analysis of three-dimensional beam structures. *International Journal for Numerical Methods in Engineering* 1979; **14**: 961–986.
49. Jonkman J, Jonkman B. NWTC Information Portal (FAST v8). https://nwtc.nrel.gov/FAST8 (Accessed 1 May 2016).
50. Guntur S, Jonkman J, Schreck S, Jonkman B, Wang Q, Sprague MA, Singh M, Hind M, Sievers R. FAST v8 verification and validation for a MW-scale wind turbine with aeroelastically tailored blades. *Proceedings of the 34th ASME Wind Energy Symposium*, San Diego, California, 2016; AIAA 2016–1008.

Pursuant to the DOE Public Access Plan, this document represents the authors' peer-reviewed, accepted manuscript.
The published version of the article is available from the relevant publisher.